

# Self-healing of Pores in PLGAs

J. Huang J<sup>a</sup>, J. M. S.P. Schwendeman<sup>b,c\*</sup>, M. D. Thouless<sup>a\*</sup>

<sup>a</sup> *Department of Mechanical Engineering and Department of Materials Science & Engineering, University of Michigan, 2350 Hayward St., Ann Arbor, MI 48109, USA.*

<sup>b</sup> *Department of Pharmaceutical Sciences and the Biointerfaces Institute, University of Michigan, NCRC, 2800 Plymouth Road, Ann Arbor, USA.*

<sup>c</sup> *Department of Biomedical Engineering, University of Michigan, 2200 Bonisteel Blvd., Ann Arbor, MI 48109, USA.*

## Abstract:

Self-healing of pores in Poly(lactic-co-glycolic acid)s (PLGA) plays an important role in the encapsulation and controlled release of drugs from PLGA microparticles. Despite the importance of this phenomenon, neither the mechanics of the deformation nor the material properties that control it have been fully studied. In this study, the material properties of PLGA have been characterized using mechanical tests, and a finite-element model has been developed to predict how pores heal. This model assumes that the healing process occurs by viscous flow resulting from the deviatoric stress field induced by the interaction between the surface curvature and the surface tension of the PLGA. The simulations, which incorporate measured material properties, show good agreement with experimental observations. However, annealing processes that occur over prolonged times increase the viscosity and slow the healing times of PLGA films at intermediate temperatures above the glass-transition temperature. These findings may be reasonably applied towards the prediction of healing processes in PLGA and in related biomaterials for important biomedical applications such as drug delivery.

## Keywords:

PLGA, Self-healing, Finite Element, Simulations, Surface Pores, Viscoelasticity.

\* Co-corresponding authors:

*E-mail address:* schwende@umich.edu; *fax:* 734-615-6162

*E-mail address:* thouless@umich.edu; *fax:* 734-647-3170

# 1. Introduction

## 1.1. Motivation

Poly(lactic-*co*-glycolic acids) (PLGA) forms the basis of some of the most widely-used biomaterials today. Since their first patented use in the 1960s, they now form key components of many products that have been approved by the US Food and Drug Administration, such as sutures (1), cardiovascular stents (2-4), skin implants (5, 6), and a plethora of drug-delivery devices such as microparticles (7-9), patches (10), and in-situ forming gels (11). Several characteristics make PLGAs attractive for medical applications. They have excellent biocompatibility, and their degradation kinetics and mechanical strengths can be easily tailored by altering molecular weights, monomer ratios, lactide isomer content, and type of end-capping. In addition, glass-transition temperatures ( $T_g$ ) near body temperature result in desirable *in vivo* release-behavior of drug-delivery systems with enhanced shelf-lives. Despite the prevalent use of PLGAs, the associated scholarly literature often does not focus on analyses of their material properties. There have been reports on the moduli of PLGA products, but very little work has been reported on the underlying physics and mechanics of the deformation behavior. An understanding of this behavior will become increasingly important as PLGA and related materials are used in new ways. Therefore, in the present work, we explore the constitutive properties of PLGA, with a focus on developing a model of the passive self-healing process in polymers.

Autonomous healing in polymers can be achieved by several different strategies. For example, “active” methods have been developed that rely on an encapsulated healing/filling agent, either in pores or in micro-vascular networks (12-15). Alternatively, in the absence of significant tensile stresses, voids and cracks in many materials can heal passively as a result of creep / viscous flow driven by surface tension. This process requires no chemical modification of the material, and relies only on the temperature being sufficiently elevated to ensure flow. This phenomenon can occur in many different applications from self-healing automotive paints (12), to erasable data storage (16). A major application of self-healing in PLGAs is the recent description of an aqueous-based micro-encapsulation method for bio-macromolecules (9). In this case, pores on the surface of PLGA microparticles self-heal to trap bio-macromolecules inside them, without the need for micronization and organic solvent exposure known to be deleterious to proteins. Similarly, healing has also been linked to the termination of the initial burst release and long-term release kinetics of PLGA-encapsulated large molecules (17, 18).

Porosity can be introduced in PLGAs as a result of phase transitions and associated density changes during curing (19). Furthermore, pore networks in PLGA microparticles can be created by the control of osmotic pressure differences induced by changes in the internal and external environments. Healing of these pores is critical for the quality of the encapsulation and release of drugs and peptides (9, 18). The healing process was explored in a series of model experiments by Mazzara et al. (20) using controlled pores that had been artificially introduced into the surface of PLGA films by blunt-tip micro-needle arrays. These experiments showed empirically that the healing times were controlled by the visco-elastic properties of the PLGA. In this present paper, we extend this work by developing a finite-element model for pore healing. The model assumes that healing proceeds by viscous flow in response to a deviatoric stress field

induced by the surface tension and curvature of the pores. The model can be used to describe pore healing in terms of the temperature and geometry. It may be useful to explain the results of past self-healing experiments. It may also be useful as the basis of a quantitative design to predict healing times corresponding to desired dosage with PLGA encapsulation.

## 1.2. Theoretical background

The underlying assumption of this model is that the pores heal by flow driven by internal stress fields established by surface tension effects (21, 22). In this section, we summarize the theoretical background of these two phenomena.

### 1.2.1. Constitutive models for a linear polymer

The simplest representation of a linear visco-elastic material is known as a Maxwell model. The constitutive behavior corresponding to such a model can be represented by a spring (with a modulus of  $E_m$ ) in series with a dashpot (with a viscosity of  $\eta_m$ ). The dashpot represents a single thermally-activated mechanism of flow, so the viscosity is of the form

$$\eta_m = \eta_{mo} e^{Q_m/RT} \quad (1)$$

where  $Q_m$  is the activation energy of the relaxation mechanism leading to flow,  $R$  is the molar gas constant,  $T$  is the absolute temperature, and  $\eta_{mo}$  is a material constant. The characteristic relaxation time ( $\tau_m$ ) of a Maxwell model is given by

$$\tau_m = \eta_m / E_m = \tau_{mo} e^{Q_m/RT} \quad (2)$$

where  $\tau_{mo}$  is a material constant. A time-dependent modulus,  $E(t)$  can be defined for a polymer as the ratio of the stress at a given time  $t$  that results from a fixed strain:

$$E(t) = E_m e^{-t/\tau_m} \quad (3)$$

The fully-relaxed modulus of a Maxwell solid, given by  $t \rightarrow \infty$ , is zero. This is important in the present context, because pore healing can only occur when the fully-relaxed modulus approaches zero.

While a Maxwell model describes some important characteristics of a polymer that exhibits pore healing, polymers generally exhibit more than one relaxation mechanism. Some of these mechanisms may allow for complete relaxation of polymer, while others may allow only partial relaxation. Each mechanism will have its own activation energy and characteristic relaxation time, and can be represented by an assembly of elements consisting of linear springs and dashpots. The time-dependent deformation of a polymer can then be modeled as the resultant of such an assembly. The individual moduli and viscosities that go into such a model are determined by fits to the observed response of the polymer at different time scales through experiments such as dynamic mechanical analyses (DMA) and stress-relaxation tests, as described below.

### 1.2.2. Role of surface energy and curvature

The chemical potential of an atom or molecule at the surface of a material depends on the product of the surface energy (surface tension) and the local surface curvature. Gradients in this potential provide a driving force for the material to change its shape, either by diffusion of atoms or molecules along the surface, or by bulk deformation in response to deviatoric (shear) stresses established within the body of the material. In the present

work, we assume that bulk flow is the dominant mechanism; this is consistent with the experimental results presented later.

The internal stress field associated with a surface (or interface) is established by the change in normal stress ( $\sigma_n$ ) across a curved surface, as given by the Young-Laplace equation:

$$\sigma_n = \gamma(\kappa_1 + \kappa_2), \quad (4)$$

where  $\gamma$  is the surface tension of the material, and  $\kappa_1$  and  $\kappa_2$  are the local principal curvatures. A convex surface results in a compressive normal stress at the surface and a concave surface results in a tensile stress at the surface. The internal stress field induced by surface curvature is exactly equivalent to the stress field induced by applied surface tractions that are normal to the surface and have a magnitude given by Equation 1. This equivalence between the stresses induced by surface curvatures and those induced by applied surface tractions forms the basis for the analysis used in this paper.

### 1.2.3. Pore healing

The healing of a surface indent is illustrated in Figure 1. The indent is initially formed by the application of a localized external pressure during indentation of a freshly-spun PLGA film. This creates large deviatoric stresses to which the polymer responds by rapidly flowing and forming an indent. The effects of surface energy at this stage are relatively small compared to the effects of the indentation stress field, so surface features such as a lip around the indent can often be retained (20). (Even when the indentations are square, the surrounding lip is approximately circular). When the indenter is removed and the film dried, deformation is driven by the deviatoric stress field that is established by the surface tension and curvatures. (A residual stress field resulting from the indentation can also contribute to this deformation; in the present work, we assume this is relaxed by flow during the indentation process.) The resulting stress field can be visualized and modeled by considering equivalent surface tractions, as shown in the schematic of Figure 1. Provided the fully-relaxed modulus is significantly smaller than the stresses induced by the surface curvature, the material can flow to smooth out any surface curvatures. Both the depth of the indent and the amplitude of any lip formed around the indent will decay over time.

For an incompressible linear-viscous material, the deformation field that results from a deviatoric stress field can be calculated using the Levy-Mises flow rule (23):

$$\frac{\dot{\epsilon}_1}{\sigma_1 - 0.5(\sigma_2 + \sigma_3)} = \frac{\dot{\epsilon}_2}{\sigma_2 - 0.5(\sigma_1 + \sigma_3)} = \frac{\dot{\epsilon}_3}{\sigma_3 - 0.5(\sigma_1 + \sigma_2)} = \frac{\dot{\tilde{\epsilon}}}{\tilde{\sigma}} = \frac{1}{3\eta}, \quad (5)$$

where  $\dot{\tilde{\epsilon}}$  and  $\tilde{\sigma}$  are the von-Mises effective strain rate and stress, and  $\dot{\epsilon}_i$  and  $\sigma_i$  ( $i = 1, 2, 3$ ) are the principal strain rates and stresses. In Mazzara et al. [12], this approach was used to develop a simple analytical result for healing an isolated spherical pore in the middle of a viscous material. The Lamé equations (23) for a spherical pore of radius  $a$  with an internal pressure of  $p = -2\gamma/a$ , give principal stresses at a distance  $r$  from the center of the pore of

$$\sigma_{rr} = \frac{2\gamma a^2}{r^3}; \sigma_{\theta\theta} = \sigma_{\phi\phi} = -\frac{\gamma a^2}{r^3}. \quad (6a)$$

The corresponding principal strain rates are given by

$$\varepsilon_{rr} = \frac{\partial u}{\partial r}; \varepsilon_{\theta\theta} = \varepsilon_{\phi\phi} = \frac{u}{r}, \quad (6b)$$

where  $u$  is the radial displacement at a distance  $r$  from the center of the pore. Recognizing that at  $r = a$ ,  $\dot{u}(a) = \dot{a}$ , and that at time  $t = 0$  the initial pore radius is  $a_o$ , it was shown [12] that the pore size is given by

$$a = a_o - \frac{\gamma t}{2\eta} \quad (7)$$

So, the time to heal a spherical pore is predicted to be  $2\eta a_o/\gamma$ .

## 2. Material and methods

### 2.1. Numerical implementation

In the numerical simulation, the initial pores were assumed to be ellipsoidal, with a depth of  $b_o$ , and a half width of  $a_o$ , on the surface of a film of thickness  $H_o$  (Figure 2). The radius of the external boundaries,  $S_o$ , were set to a value of  $S_o/a_o = 10$  in all simulations. It was demonstrated numerically that this value was large enough so that its effect was always limited to less than a 2% error in the calculated pore depth. The bottom of the film was assumed to be attached to a rigid substrate, but free to expand. The assumption of axisymmetric geometries allowed the calculations to be simplified, while retaining the essential elements of the experimental studies. Furthermore, since the stresses are dependent on local curvatures, there is a very large driving force for any sharp corners to be rounded out. This results in a transition to axisymmetric shapes early in the healing process, so that details of the initial geometry have only a limited effect on the healing time. Indeed, Mazzara *et al.* (20) reported that their initially square pores quickly became circular. We used our numerical method to analyze cylindrical pores, and they evolved fairly quickly into ellipsoidal shapes. However, the initial sharp corners in a cylindrical void requires a very dense mesh for finite-element analyses. Therefore, ellipsoidal geometries were used to model the pores in the general cases presented in this paper.

Finite-element analyses were conducted using the commercial package ABAQUS. The stress fields resulting from the surface tension were induced in the finite-element model by applying tractions to the surface proportional to the sum of the principal curvatures (Equation 4). A numerical technique for calculating the curvatures has been described by Henann *et al.* (24). We used a similar approach to calculate the curvatures of the axisymmetric surfaces. Such a surface can be described by  $z = Z(r)$ , where  $z$  is the height above an arbitrary reference value, and  $r$  is the distance from the axis of symmetry. The sum of the two principal curvatures (twice the mean curvature) at any point on the surface is given by

$$2\kappa = \kappa_1 + \kappa_2 = \frac{\partial^2 Z/\partial r^2}{[1 + (\partial Z/\partial r)^2]^{3/2}} + \frac{\partial Z/\partial r}{r[1 + (\partial Z/\partial r)^2]^{1/2}}. \quad (8)$$

Thus, the calculation is reduced to a two-dimensional problem. The coordinates of an integration point  $A$  ( $r_A, z_A$ ), and the coordinates of its two nearest neighboring integration

points,  $B (r_B, z_B)$  and  $C (r_C, z_C)$ , can be fitted to a parabola ( $y'/y_o = x^2$ ) in terms of a local coordinate system with an origin located at point  $A$  and aligned with the local normal direction. The sum of the principal curvatures at  $A$  is then given by

$$2\kappa = 2y_o - n_r/r, \quad (9)$$

where  $n_r$  is the radial component of the outward normal vector at  $A$ . This procedure was used to calculate the curvature, and the corresponding surface tractions, at all points on a surface. A DLOAD user-subroutine was developed and implemented in ABAQUS/Standard. The user-subroutine was verified using the simple geometries of a sphere and a cylinder. Mesh and boundary sensitivity studies were conducted empirically by changing the size of the mesh and the distance to remote boundaries, and verifying that any influence on the results was significantly less than uncertainty associated with the measurements of the material parameters.

## 2.2. Material preparation

PLGA 50:50 with lauryl-ester-terminated chains, with a weight-averaged molecular weight of 55.3 kDa, and average inherent viscosity of 0.61 dL g<sup>-1</sup> was provided by Lactel Inc. Details of the preparation of the PLGA films were reported by Mazzara et al. (20). Briefly, the polymer was dissolved in acetone (27% w/w), and spin-coated onto a Teflon-coated glass substrate. The films were dried for one day in a fume-hood at room temperature, and then for an additional day under vacuum at room temperature to remove excess solvent. When the films were separated from the glass substrate they had a final thickness of 16 ± 3 μm (n=3, ± Standard Deviation).

## 2.3. Material characterization

### 2.3.1. Stress-relaxation tests

Dry films were cut into rectangular specimens of approximately 10 mm in width and 30 mm in length. Stress-relaxation tests were conducted in a temperature range of 40 °C to 65 °C using a TA Instruments RSA3 dynamic mechanical analyzer. The samples were placed in the grips at room temperature and heated to the desired temperature at 100 °C min<sup>-1</sup>. One minute was allowed for the temperature to stabilize before a strain of 3 % was applied within 5 ms. The strain was held constant, and the corresponding stress was then measured every 0.01 second.

### 2.3.2. Dynamic mechanical analysis

The same instrument was used to measure the visco-elastic properties of the PLGA films by dynamic mechanical analysis (DMA). Samples were tested in uniaxial tension at a frequency of 1 Hz, with a strain amplitude of 0.1% and an initial mean force of 0.01 N. The storage modulus,  $E'$ , loss modulus,  $E''$ , and loss tangent,  $\tan\delta$ , were measured over a temperature range of 25 °C to 70 °C, with a temperature ramp-up rate of 3 °C min<sup>-1</sup> and a soak time of 30 seconds to reach steady state at each temperature. Three identical samples were analyzed to determine representative values and uncertainties.

Frequency sweep tests in the range of 0.001 Hz to 99 Hz with a strain amplitude of 0.1% were then conducted in a temperature range of 25 °C to 65 °C. The mean strains in these cyclic tests were set to be 25% greater than the strain amplitudes to ensure that

the specimen never went into compression. The storage modulus, loss modulus and  $\tan\delta$  were determined as functions of frequency.

### 2.3.3. Measurement of surface tension

The surface tensions of the PLGA films were determined by placing a drop of water on the films and using a goniometer to measure the polymer-water contact angle. Contact angles for each film were measured in three distinct locations, and a minimum of two samples were used for each set of conditions. The contact angles were used to calculate the tension,  $\gamma$ , following Berthelot's combining rule (25)

$$\gamma = (1 + \cos\theta)^2 \gamma_w / 4 \quad , \quad (10)$$

where  $\theta$  is the contact angle, and  $\gamma_w$  is the surface tension of the water.

### 2.3.4. The effects of annealing and the kinetics of solvent escape

To investigate the effects of annealing and annealing time on the visco-elastic properties of the PLGA, films were incubated at three temperatures (50 °C, 55 °C and 65 °C) above the  $T_g$  for various times. The properties of these films were tested using DMA and relaxation tests, as described above.

To quantify the kinetics of annealing and solvent escape, the films were subjected to thermo-gravimetric analysis (TGA). Approximately 20 mg of PLGA was placed on platinum pans and quickly heated (50 °C/min) to 50 °C, 55 °C and 65 °C. The films were held isothermally for 8 hours, and the percent change in mass was recorded. Note that glass-transition temperature data for these films were reported in our previous work (20).

## **3. Results**

### *3.1. Validation of finite-element model*

Equation (7) gives the analytical solution for the radius of a spherical pore in an infinite body of an incompressible Maxwell solid as a function of time. As a check on the validity of our numerical technique, we repeated this calculation numerically, using the finite-element model discussed above. A comparison between the simulation and the analytical results is presented in Figure 3, showing that the finite-element model gives the expected result. It should be noted that, in this case, the numerical calculations suffer from excessive distortion of the mesh when the pore is very small, owing to the huge normal stresses acting at the surface. For this reason, the numerical calculations shown in Figure 3 could not be taken all the way to complete pore healing.

### *3.2 Numerical results for surface pores*

Figure 4(a) shows how the depth of an initially ellipsoidal surface pore evolves with time for a Maxwell material. It should be noted that, in contrast to the healing of a spherical pore inside a polymer, the depth of the pore goes to zero only asymptotically. There is no well-described healing time. Instead, the healing time must be defined in terms of how long a pore takes to heal to a given percentage of its original depth. Experimentally, this will be the depth at which the pore can no longer be distinguished. Unless stated otherwise, we use a fixed percentage of 85% to define healing in the numerical simulations, since this corresponds to the point at which the healing rate starts to decay markedly. This arbitrary definition introduces a systematic error into absolute

comparisons with experimental data for healing times; however, it is expected that relative comparisons will be unaffected as all the simulations will be affected equally.

The change in the cross-sectional profile of an axisymmetric surface pore with time is shown in Figure 4b. This set of images corresponds to the simulation for which  $a_o/b_o = 1$  in Figure 4a. The full animated clip from which these images are taken can be found in the supplementary material.

### 3.3. *Effect of temperature on healing of wet films*

We did not have the capability to do DMA and stress-relaxation tests in an aqueous environment. However, the results presented by Mazzara *et al.* (20) for the healing of pores in wet films as a function of temperature were used as a preliminary validation of the physics of the model. An activation energy of  $193 \text{ kJ mol}^{-1}$  for the viscosity of the wet PLGA films was found by fitting the healing data to an Arrhenius plot in Ref. (20). This value of activation energy was used in our finite-element calculations, with a representative value of Young's modulus  $E = 1 \text{ GPa}$ . (This choice of modulus was not important for the calculations, but it is consistent with the measured value for a dry PLGA film, as described later.) It is important to note that the activation energy and  $T_g$  of these hydrated films were suppressed compared to those of the dry films, owing to plasticization of the polymer by water (20).

The pores in the wet PLGA had an initially square cross section, and an initial width-to-depth ratio of  $a_o/b_o = 5/14$ . By fitting the observed healing time for these pores at one arbitrarily chosen temperature of  $53 \text{ }^\circ\text{C}$  to the numerical predictions for ellipsoidal pores with the same aspect ratio to heal to 85%, and using an activation energy of  $193 \text{ kJ mol}^{-1}$  for the viscosity, a value for  $\gamma/\eta_o$  could be determined as  $7.9 \pm 2.3 \times 10^{21} \text{ m s}^{-1}$ . This fitted value of  $\gamma/\eta_o$  was then used in conjunction with the activation energy of  $193 \text{ kJ mol}^{-1}$  for the viscosity in the finite-element model to calculate the healing time for identical pores over a range of temperatures. A comparison between the predicted healing times and the temperature is shown in Figure 5a.

The role of the initial aspect ratio and volume on healing time was also investigated experimentally in Ref. [19]. The material parameters described above were incorporated into a finite-element calculation, and used to predict the healing time (again, defined as an 85% reduction in depth) for differently shaped pores. These predictions are shown in Figure 5b, and compared with the experimental observations. It should be emphasized that this comparison, unlike that of Figure 5a, does not reflect any fits to the data. Therefore, the reasonable agreement between the predictions and experimental results provides support for the modeling.

### 3.4. *Measurement of properties for dry PLGA films*

#### 3.4.1. Stress relaxation

In the study described above, the material properties for wet PLGA films were determined from fits to experimentally observed data, and then used to calculate pore healing. While this shows consistency between the model and the experimental observations, a much more important question is whether it is possible to measure the material properties independently of the pore-healing experiments, and to use these

properties in a numerical model to predict the healing behavior. This was the goal of the studies on the dry PLGA films for which it was possible to measure the properties.

An initial assumption was that the PLGA behaves in these stress-relaxation tests as a simple Maxwell solid with a time-dependent modulus as given by Equation 3. This equation shows that a log-linear plot of the time-dependent modulus against time should be of the form of a straight line with a slope of  $-\tau_m$ .

Experimental plots for the time-dependent modulus are shown in Figure 6(a) for the temperature range of 40 °C to 65 °C. These plots show a very fast initial relaxation of the time-dependent modulus followed by a slower decrease. If we assume that PLGA is a linear polymer, this initial rapid drop indicates at least one additional relaxation mechanism with a relatively short time constant. The time constant for this fast relaxation was too small to be extracted reliably from the stress-relaxation data of Figure 6(a); however, it was determined by means of DMA, as described later. At longer time scales, there does appear to be a single dominant mechanism that gives a constant slope to the stress-relaxation curves. The slopes of these lines corresponding to different temperatures were determined by a least-squares fit process, and plotted on an Arrhenius plot in the form of  $\log(\tau_m)$  against  $1/T$  in Figure 6(b). The slope of this line indicates an activation energy of  $Q_m = 206 \pm 6 \text{ kJ mol}^{-1}$ , and a pre-exponential term of  $\tau_{mo} = 6.4 \pm 0.2 \times 10^{-32} \text{ s}$ . It can be observed that at all temperatures, the constant slope at long time scales starts when the time-dependent modulus is in the range of  $1.5 \pm 0.5 \text{ MPa}$ . Using this value of the modulus for  $E_m$  in the Maxwell model, Eqns. (1) and (2) can be used to deduce a value of  $\eta_{mo} = 9.6 \pm 3.5 \times 10^{-32} \text{ MPa}\cdot\text{s}$ .

### 3.4.2. Dynamic mechanical analysis

The storage modulus and loss tangent for dry PLGA films computed from DMA temperature-sweep tests at 1 Hz are plotted in Figure 7(a). From this plot, the unrelaxed modulus is estimated to be  $1.6 \pm 0.3 \text{ GPa}$ , being the asymptotic level that the storage modulus tends to at low temperatures. It should be noted from Figure 7(a) that the peak in  $\tan\delta$  is a double peak. The first peak is at about 38 °C, which is consistent with the estimate of Mazzara *et al.* (20) for a  $T_g$  between 35 °C and 40 °C. Here, we will neglect the fine details of the relaxation peak, and assume a single relaxation mechanism that operates at 1 Hz over the temperature range of 38 °C to 48 °C.

To extract the visco-elastic properties of the relaxation mechanisms that caused the fast initial relaxations observed in the stress relaxation tests, we conducted frequency sweep tests. Representative results of the tests are shown in Figure 7(b). The results show single peaks in the loss modulus, and they can be interpreted based on a standard-linear-solid (SLS) model. Such a model results in a time-dependent modulus of the form (26)

$$E(t) = E_r + E_s e^{-t/\tau_s} \quad (11)$$

In this equation, the fully-relaxed modulus,  $E(\infty)$ , is given by  $E_r$ , and the unrelaxed modulus,  $E(0)$  is given by  $E_r + E_s$ . The temperature-sweep tests gave a value for this unrelaxed modulus of  $E(0) = 1.6 \pm 0.3 \text{ GPa}$ .

A standard-linear solid also has a viscosity of the form  $\eta_s = \eta_{s0} \exp(Q_s / RT)$ , where  $Q_s$  is the activation energy and  $\eta_{s0}$  is a material constant. The storage modulus,  $E'(\omega)$ , and loss modulus,  $E''(\omega)$ , of an SLS are given by (26):

$$E'(\omega) = E_r + E_s \frac{\omega^2 \tau_s^2}{1 + \omega^2 \tau_s^2} \quad (12a)$$

$$E''(\omega) = E_s \frac{\omega \tau_s}{1 + \omega^2 \tau_s^2} \quad (12b)$$

where  $\omega$  is the angular frequency of the input strain, and the time constant is  $\tau_s = \eta_s / E_s$ . The loss modulus is maximal at  $\omega = 1/\tau_s$ , so the time constants at different temperatures can be extracted from the peaks in the loss modulus. These are plotted as an Arrhenius plot in Figure 7(c). From this plot, the activation energy was determined to be  $Q_s = 250 \pm 29 \text{ kJ mol}^{-1}$ , and the pre-exponential term,  $\tau_{s0} = \eta_{s0} / E_s$ , was determined to be  $6.6 \pm 0.8 \times 10^{-44} \text{ s}$ .

The fully-relaxed modulus,  $E_r$ , of a standard-linear solid can be determined from the difference between the storage and loss modulus at the frequency corresponding to the maximum loss modulus (Equation 12). In the present case, there was a slight dependence of the relaxed modulus on temperature. This indicates the presence of additional fast relaxation mechanisms, which are ignored in the present analysis. However, the relaxed moduli measured from the peaks in the loss modulus are consistent with the value of  $1.5 \pm 0.5 \text{ MPa}$  determined from the stress-relaxation experiments for  $E_m$ .

Combining the results from the stress-relaxation tests and the frequency-sweep tests, we propose a material model for dry PLGA films as shown in Figure 8(a). The model consists of a standard-linear solid in series with a dashpot, and has a time-dependent modulus of

$$E(t) = \left( E_r + E_s e^{-t/\tau_s} \right) e^{-t/\tau_m} \quad (13)$$

In this model, the standard-linear solid provides a time-dependent initial modulus for the Maxwell dashpot. The parameters for the different elements of the model are summarized in Table 1. The Maxwell dashpot with a viscosity of  $\eta_m$  dominates the healing process and is the one we are particularly interested in when analyzing the healing process. The dashpot associated the standard-linear solid, with a viscosity,  $\eta_s$ , is associated with relaxing 99.9% of the instantaneous modulus, but it has no significant effect on healing. When this model is used in a finite-element code, it needs to be converted to the form shown in Figure 8(b), which is the equivalent Prony-series representation. In this figure,  $E_1 = E_s$ ,  $E_2 = E_m$ ,  $\eta_1 = (1/\eta_s + 1/\eta_m)^{-1}$ , and  $\eta_2 = \eta_m$ . A Prony-series representation requires a non-zero fully-relaxed modulus. Therefore, an arbitrary value of  $E_3$  was chosen that was sufficiently low so as not to impede the healing.

### 3.4.3. Interfacial tension for dry PLGA

The water-polymer contact angle for the PLGA films used above was measured to be  $71.8 \pm 1.4^\circ$ . Using the Berthelot combining rule and a water-air interfacial tension of  $72.70 \text{ mN m}^{-1}$  (25), the surface energy of dry PLGA films was calculated to be  $\gamma = 31.0 \pm 2.0 \text{ mN m}^{-1}$ .

### 3.5. Prediction on healing times for pores in dry PLGA films

Finite-element calculations of pore healing in dry PLGA films using the material properties described above were performed. Axisymmetric ellipsoidal pores with an aspect ratio  $a_o / b_o = 2.5/7$  and a pore volume of  $91.6 \text{ }\mu\text{m}^3$  were used to match the values from the experimental study (20). The predicted healing times are plotted as a function of temperature in Figure 9, along with the experimental results. Three different contours of different healing levels are plotted in Figure 9, showing the effect of small changes in the definition of healing.

## 4. Discussion

While Figure 9 shows that the numerical predictions are generally consistent with the experimental observations, the experimental healing times appear to be significantly longer than expected at lower temperatures. It is conjectured that this is a result of changes in material properties associated with annealing, as a result of relatively long healing times at low temperatures. In particular, the films used in the study had significant residual solvent content. This excess solvent acts as a plasticizer for the polymer, effectively decreasing its viscosity and  $T_g$  (27). Consequently, any loss of this solvent over long periods of times may cause an increase in the viscosity and  $T_g$  and a corresponding increase in the healing times. This is consistent with the common observation of a higher  $T_g$  during the second heating cycle of differential scanning calorimetry (20).

To elucidate the effects of annealing, samples of the PLGA were held isothermally in a TGA experiment for 8 hours at temperatures of  $50^\circ\text{C}$ ,  $55^\circ\text{C}$  and  $65^\circ\text{C}$  (Supplementary Figure 1). The initial rate of solvent evaporation increased with temperature. However, after two hours, there was no significant further evaporation, and the final weight loss indicated that the initial residual solvent content had been about 1.7%. The weight loss during the first one hour was fitted to the equation:

$$w_{\text{loss}}(t) = C_1(1 - e^{-At}) \quad , \quad (14)$$

where  $C_1$  is a constant, which is the asymptotic value of the weight of the evaporated solvent at long time scales, and  $A$  is a temperature-dependent rate parameter. By fitting the data within the first hour (when most drastic weight loss occurs) using Equation 14, and plotting the parameter  $A$  on an Arrhenius plot, the activation energy of this solvent escape process was determined to be  $55 \pm 1.3 \text{ kJ mol}^{-1}$ .

The most important visco-elastic property of the films, from the perspective of pore healing, is the viscosity represented by the second dashpot ( $\eta_m$ ) in Figure 8a. The effects of annealing on viscosity were investigated by holding the films isothermally at  $65^\circ\text{C}$  for up to two hours. DMA was then used to measure the  $T_g$ , and stress-relaxation measurements were used to determine the viscosity. These results showed that annealing

raised the  $T_g$ , increased the viscosity and dropped the activation energy, but the instantaneous modulus was not significantly affected. These changes are summarized in Table 2 for different annealing times at 65 °C. It should be noted that the time scales over which the relaxation data were obtained (see Figure 6a, for example) were much smaller than the time scales over which significant annealing might occur. Therefore, it is believed that annealing did not occur while the relaxation data were being collected.

In addition to changes in the bulk properties of the PLGA, measurements of the contact angle suggested that the polymer-air interfacial tension may also change significantly as a result of solvent evaporation and annealing. In particular, annealing at 65 °C for two hours gradually reduced the interfacial tension from  $31 \pm 2 \text{ mN m}^{-1}$  to  $25 \pm 3 \text{ mN m}^{-1}$ .

Finite-element simulations of pore healing were performed using the most extreme values of the material properties given in Table 2 (to provide an upper bound on the healing time). These results are presented in Figure 10. As can be seen from this figure, while the use of the unannealed properties provide excellent predictions for the behavior at high temperatures, the use of annealed properties provide better predictions at the lower temperatures. At the higher temperatures, the total time required to heal the film is comparable to the annealing time, so most of the healing occurs before full annealing. However, at lower temperatures, the time scales for annealing are smaller than the time scales for healing, so the results are more affected by the annealing. This is expected since the activation energy for solvent evaporation of  $55 \pm 1.3 \text{ kJ mol}^{-1}$  is smaller than the activation energy for viscous flow. The differences between the simulations for an annealed and unannealed film reflect different values for surface tension, viscosity, and  $T_g$ , all of which appear to change during annealing of a film.

In many materials, surface pores can also heal by surface diffusion; for example, this is the mechanism often ascribed to the healing of pores in high-temperature ceramics (28-30). However, this does not appear to be the case for PLGA. First, the healing data does seem to be quite well described by the visco-elastic properties of the PLGA. Second, surface diffusion tends to have a lower activation energy than the bulk diffusive processes responsible for flow. This would decrease the healing time at low temperatures below that predicted from viscous flow. The opposite trend was observed, so the discrepancy in healing times is not a result of surface diffusion; rather it is a result of solvent evaporation, as discussed above.

Finally it is interesting to consider how these changes might correlate to pore healing in PLGA microparticles. These are generally dried to remove excess water and solvent, so there is expected to be a low solvent content during incubation. However, water is known to plasticize PLGA so, upon hydration of the polymer, the glass-transition temperature would drop, as it does in the presence of residual solvent. Furthermore, the pores in the microspheres can vary considerably in size, from 10 nm up to 10  $\mu\text{m}$ . These compound effects of variability in  $T_g$  and a range of pore sizes, would make the application of the analysis presented here to PLGA microspheres a logical application to model the influence of healing on the long-term release of macromolecules.

## 5. Conclusions

Self-healing in PLGA can be modelled by flow driven by internal stress fields established by surface-tension effects. A finite-element model incorporating a numerical method to calculate the evolution of surface curvatures was developed to analyze indent healing in visco-elastic materials. The rate of healing surface pores decreases as the pores heal, with the pore depth approaching zero asymptotically. The visco-elastic properties of PLGA films were characterized using a combination of DMA and stress-relaxation tests. The dry PLGA films used in this study had a relatively high instantaneous modulus of  $1.6 \pm 0.3$  GPa, and a glass transition temperature of  $38.4 \pm 0.3$  °C, owing to reduced solvent content. The PLGA displayed relaxation mechanisms with at least two distinct time scales. The first mechanism is a fast one with a very short time constant; this reduced the modulus by 99.9% at a time scale of less than a minute at temperatures above glass transition temperature, leaving the film with a partially-relaxed modulus of  $1.5 \pm 0.5$  MPa. This modulus, although much smaller than the instantaneous modulus, is still too large for healing to occur. A second relaxation mechanism with a much longer time constant was responsible for viscous flow that could accommodate pore healing.

Finite-element simulations of indent healing using material properties that had been independently measured were broadly consistent with earlier experimental observations reported by Mazzara et al. (20). It was noted that annealing of the films, which is associated with solvent evaporation, resulting in longer healing times than expected at lower temperatures.

Since the healing mechanism is thermally activated, temperature is one of the most important factors in self-healing of PLGA. The temperature needs to be high enough for viscous flow to occur during the time scales of interest. In addition to the temperature, the indent geometry also affects healing time, with larger indents requiring longer time to heal. While this present study has focused on the healing of indents as a model for surface pores in PLGA films, we believe that the numerical tools used to analyze the process and the experimental techniques used to deduce the relevant material properties will be appropriate for predicting the pore-healing processes of significance for pharmaceutical use of these materials.

### **Acknowledgements:**

This work was partially supported by NIH R21 EB 08873. Graduate-student support for JMM was provided by the PhRMA Foundation's pre-doctoral fellowship in Pharmaceutics. Graduate-student support for JH was provided by the Department of Mechanical Engineering, University of Michigan. The authors would like to thank Prof. Kristen Mills for her help in developing the user-subroutine.

## References

1. Schmitt EE, Polistina RA. *Surgical sutures* 1967.
2. Klugherz BD, Jones PL, Cui X, Chen W, Meneveau NF, DeFelice S, Connolly J, Wilensky RL, Levy RJ. Gene delivery from a DNA controlled-release stent in porcine coronary arteries. *Nature Biotechnology*. 2000;18(11):1181-4.
3. Wang X, Venkatraman SS, Boey FYC, Loo JSC, Tan LP. Controlled release of sirolimus from a multilayered PLGA stent matrix. *Biomaterials*. 2006;27(32):5588-95.
4. Pan CJ, Tang JJ, Weng YJ, Wang J, Huang N. Preparation and characterization of rapamycin-loaded PLGA coating stent. *Journal of Materials Science: Materials in Medicine*. 2007;18(11):2193-8.
5. Patrick Jr CW, Zheng B, Johnston C, Reece GP. Long-term implantation of preadipocyte-seeded PLGA scaffolds. *Tissue Engineering*. 2002;8(2):283-93.
6. Wang Y, Ameer GA, Sheppard BJ, Langer R. A tough biodegradable elastomer. *Nature Biotechnology*. 2002;20(6):602-6.
7. Hans ML, Lowman AM. Biodegradable nanoparticles for drug delivery and targeting. *Current Opinion in Solid State and Materials Science*. 2002;6(4):319-27.
8. Cheng J, Teply BA, Sherifi I, Sung J, Luther G, Gu FX, Levy-Nissenbaum E, Radovic-Moreno AF, Langer R, Farokhzad OC. Formulation of functionalized PLGA-PEG nanoparticles for in vivo targeted drug delivery. *Biomaterials*. 2007;28(5):869-76.
9. Reinhold SE, Desai KGH, Zhang L, Olsen KF, Schwendeman SP. Self - healing microencapsulation of biomacromolecules without organic solvents. *Angewandte Chemie International Edition*. 2012;51(43):10800-3.
10. Park JH, Allen MG, Prausnitz MR. Biodegradable polymer microneedles: fabrication, mechanics and transdermal drug delivery. *Journal of Controlled Release*. 2005;104(1):51-66.
11. Ghahremankhani AA, Dorkoosh F, Dinarvand R. PLGA-PEG-PLGA tri-block copolymers as in situ gel-forming peptide delivery system: effect of formulation properties on peptide release. *Pharmaceutical Development and Technology*. 2008;13(1):49-55.
12. van Benthem RATM, Ming W, de With G. Self-healing polymer coatings. *Self Healing Materials*. 2008:139-59.
13. Wilson GO, Andersson HM, White SR, Sottos NR, Moore JS, Braun PV. Self-healing polymers. *Encyclopedia of Polymer Science and Technology*: John Wiley & Sons, Inc.; 2002.
14. Cho SH, White SR, Braun PV. Self - Healing Polymer Coatings. *Advanced Materials*. 2009;21(6):645-9.
15. Toohey KS, Sottos NR, Lewis JA, Moore JS, White SR. Self-healing materials with microvascular networks. *Nature Materials*. 2007;6(8):581-5.
16. Vettiger P, Cross G, Despont M, Drechsler U, Durig U, Gotsmann B, Haberle W, Lantz MA, Rothuizen HE, Stutz R. The 'millipede'-nanotechnology entering data storage. *IEEE Transactions on Nanotechnology*. 2002;1(1):39-55.
17. Wang J, Wang BM, Schwendeman SP. Characterization of the initial burst release of a model peptide from poly (D, L-lactide-co-glycolide) microspheres. *Journal of Controlled Release*. 2002;82(2):289-307.

18. Kang J, Schwendeman SP. Pore closing and opening in biodegradable polymers and their effect on the controlled release of proteins. *Molecular Pharmaceutics*. 2007;4(1):104-18.
19. Nakahara S. Microporosity in thin films. *Thin Solid Films*. 1979;64(1):149-61.
20. Mazzara JM, Balagna MA, Thouless MD, Schwendeman SP. Healing kinetics of microneedle-formed pores in PLGA films. *Journal of Controlled Release*. 2013;171(2):172-7.
21. Packard CE, Schroers J, Schuh CA. In situ measurements of surface tension-driven shape recovery in a metallic glass. *Scripta Materialia*. 2009;60(12):1145-8.
22. Kumar G, Schroers J. Write and erase mechanisms for bulk metallic glass. *Applied Physics Letters*. 2008;92(3):031901.
23. Chakrabarty J. *Theory of plasticity*: Butterworth-Heinemann; 2006.
24. Henann DL, Anand L. Surface tension-driven shape-recovery of micro/nanometer-scale surface features in a Pt (57.5) Ni (5.3) Cu (14.7) P (22.5) metallic glass in the supercooled liquid region: A numerical modeling capability. *Journal of the Mechanics and Physics of Solids*. 2010;58(11):1947-62.
25. Kwok DY, Neumann AW. Contact angle measurement and contact angle interpretation. *Advanced Colloidal Interfaces*. 1999;81(3):167-249. doi: Doi 10.1016/S0001-8686(98)00087-6. PubMed PMID: ISI:000082127900001.
26. Lakes RS. *Viscoelastic Materials*. Cambridge: Cambridge University Press; 2009.
27. Sperling LH. Introduction to Physical Polymer Science, 4th Edition. *Introduction to Physical Polymer Science*, 4th Edition. 2006:1-845. PubMed PMID: ISI:000298543000017.
28. Evans AG, Charles EA. Strength recovery by diffusive crack healing. *Acta Metallurgica*. 1977;25(8):919-27.
29. Rödel J, Glaeser AM. High - Temperature Healing of Lithographically Introduced Cracks in Sapphire. *Journal of the American Ceramic Society*. 1990;73(3):592-5601.
30. Smith DL, Evans B. Diffusional crack healing in quartz. *Journal of Geophysical Research: Solid Earth*. 1984;89(B6):4125 -- 35.

## Tables

**Table 1** Values of parameters of the unannealed dry PLGA (see Fig. 8a).

$E_s$ (MPa)	$(1.6 \pm 0.3) \times 10^3$
$E_r$ (MPa)	$1.5 \pm 0.5$

	$\eta_o$ (MPa·s)	$Q$ (kJ/mol)
$\eta_s$	$(1.1 \pm 0.3) \times 10^{-40}$	$250 \pm 29$
$\eta_m$	$(9.6 \pm 3.5) \times 10^{-32}$	$206 \pm 6$

**Table 2** Effect of annealing on the dry PLGA parameters at 65°C.

Annealing time (hours)	$T_g$ (°C)	$\eta_{mo}$ (MPa·s)	$Q_m$ (kJ/mol)
<b>0</b>	$38.4 \pm 0.3$	$(9.6 \pm 3.5) \times 10^{-32}$	$206 \pm 6$
<b>0.5</b>	$47.0 \pm 0.3$	$(2.0 \pm 0.2) \times 10^{-20}$	$140 \pm 10$
<b>1</b>	$49.5 \pm 0.3$	$(2.0 \pm 0.2) \times 10^{-22}$	$150 \pm 10$
<b>2</b>	$50.8 \pm 0.3$	$(2.8 \pm 0.2) \times 10^{-22}$	$150 \pm 10$

## Figure Captions

- Figure 1** Self-healing in PLGA. **a)** A schematic illustration of the healing process showing the shape-recovery of a surface pore driven by stress fields arising from surface curvature. The stress fields can be mimicked by the application of surface tractions that are proportional to local curvatures. **b)** Micrographs of self-healing of pores introduced by indentation of a PLGA film when incubated at 65 °C. **c)** Self-healing of surface pores in PLGA microparticles used in controlled release. The left image is after fabrication using the solvent evaporation method as previously described (9), and the right image is after incubation in solution at 42 °C (above  $T_g$ ) for 48 hours.
- Figure 2** **a)** A schematic illustration of an axisymmetric ellipsoidal surface pore. **b)** The axisymmetric geometry used in the numerical simulations. The boundaries are located at an outer radius of  $S_o$ , which is big enough so that the pore can be considered as an isolated pore. The thickness of the substrate is  $H_o$ . The bottom symmetry plane models free sliding on a rigid substrate.
- Figure 3** The results of a numerical calculation of the healing time of a spherical pore in infinite visco-elastic body agree with the analytical results. The numerical results are affected by the excessive distortion when the residual radius of the pore is small, resulting in larger uncertainties, as represented by the error bars.
- Figure 4** **(a)** Numerical results showing how the residual depth of an ellipsoidal surface pore in a Maxwell material varies as a function of time; these results illustrate how the rate of healing slows down as the pore depth decreases. In this plot, the time,  $t$ , has been normalized by the surface tension,  $\gamma$  the viscosity,  $\eta$ , and the initial volume of the pore,  $V_o$ . Wider and shallower pores, of the same initial volume require longer times to reach the same level of healing. The error bars on these plots correspond to numerical uncertainties associated with mesh size. **(b)** Numerical results showing how the cross-sectional profile of a surface pore evolves with time. This images are taken from the simulation used to generate the data of Figure 4a, with  $a_o/b_o = 1$ .
- Figure 5** **(a)** A comparison between the calculated time to heal pores in a wet PLGA film ( $T_g = 23.4 \pm 0.4$  °C) and the experimental observations of Mazzara *et al.* (20), as a function of temperature. The geometrical parameters of the ellipsoidal pore used in the numerical calculations were  $a_o/b_o = 5/14$ ,  $S_o/a_o = 10$ , and  $H_o/b_o = 25/7$ . These were consistent with the experimental geometries that had pores with an initially square cross section. The material properties were chosen to fit the experimental results at 53 °C, and an activation energy of 193 kJ mol<sup>-1</sup> for the viscosity had been previously estimated from an Arrhenius fit to these data (20). The uncertainty in the numerical simulations (represented by the dashed

lines) matches the uncertainty from the experimental results at 53 °C. **(b)** Good agreement is shown between the predicted and experimentally-observed effects of pore volume and aspect ratio on healing time. The experimental data are from Mazzara *et al.* [19], and the parameters for the numerical studies were identical to those used for Figure 5(a). The uncertainty in the numerical simulations (represented by the dashed lines) comes from the uncertainties to the fit in Figure 5(a).

**Figure 6** **(a)** Sample data of stress relaxation tests for dry PLGA films at different temperatures for an initial strain of 3%, using a TA Instruments RSA3 dynamic mechanical analyzer. While the plot for a single thermally-activated relaxation is a straight line, the initial change in slope indicates additional rapid relaxation mechanisms. Only the longer-scale relaxation data were obtained from this plot. The constant slope associated with this longer time scales starts when the time-dependent modulus is  $1.5 \pm 0.5$  MPa. **(b)** The time constant,  $t_m$ , obtained from the data of Figure 6(a) decreases as the temperature,  $T$ , increases. An Arrhenius plot of relaxation time against  $1/T$  shows an activation energy of  $206 \pm 6$  kJ mol<sup>-1</sup> for the viscosity term responsible for the slow relaxation in the temperature range of 40 °C to 65 °C. The data also indicate that the pre-exponent for the time constant (Equation 2) is given by  $t_{m0} = 6.4 \pm 0.2 \times 10^{-32}$  s.

**Figure 7** **(a)** Temperature dependence of storage modulus and loss tangent determined by DMA for dry PLGA films. The tests were conducted at a constant frequency of 1 Hz. Three samples were tested, and the average value has been plotted. The double peaks in  $\tan\delta$  indicate at least two relaxation mechanisms with similar time constants in the temperature range, which can be approximated by one equivalent dashpot. The unrelaxed storage modulus is estimated to be  $1.6 \pm 0.3$  GPa. **(b)** Representative data from DMA frequency sweep test showing the storage and loss modulus as functions of frequency for dry PLGA films at 30 °C. The loss modulus presents with a single peak within the range of frequency analyzed, and can be interpreted based on a standard linear solid model. The time constant can be calculated from the peak in the loss modulus, as explained in the text. **(c)** The time constant obtained from data such as that shown in Fig 7b decreases as the temperature,  $T$ , increases. An Arrhenius plot shows an activation energy of  $250 \pm 29$  kJ mol<sup>-1</sup> for the fast relaxation. The pre-exponent for the time constant (Equation 2) is given by  $\tau_{s0} = 6.6 \pm 0.8 \times 10^{-44}$  s.

**Figure 8** Proposed material model for PLGA. **(a)** The model consists of a standard linear solid in series with a dashpot. The standard linear solid series provide a time-dependent initial modulus for the lower dashpot. The material has a fully-relaxed modulus of zero, ensuring complete healing to occur. The lower dashpot is the dominant relaxation mechanism at longer time scales. **(b)** The equivalent model used as a Prony series for finite

element calculations in ABAQUS, with  $E_1 = E_s$ ,  $E_2 = E_r$ ,  $\eta_1 = (1/\eta_s + 1/\eta_m)^{-1}$ , and  $\eta_2 = \eta_m$ .  $E_3$  was arbitrarily chosen for the implementation of the Prony series, and was sufficiently small so as not to impede healing.

**Figure 9** The predicted time to heal a surface pore in dry PLGA films, using the material properties obtained in this study. Three different definitions of healing, 83%, 85% and 87% are shown to illustrate the sensitivity of the results to the definition of healing. The predicted results are in good agreement with the experimental observations at high temperatures, but predict too short a healing time at lower temperatures.

**Figure 10** The predicted time to heal a surface pore in annealed PLGA films, using the annealed properties of the PLGA. The annealed properties provide a better match for the predictions at low temperatures, while the un-annealed properties provide a better match at higher temperatures. This is consistent with the notion that the long healing times at low temperatures allow annealing to occur, and the corresponding loss of solvent reduces the viscosity of the PLGA.

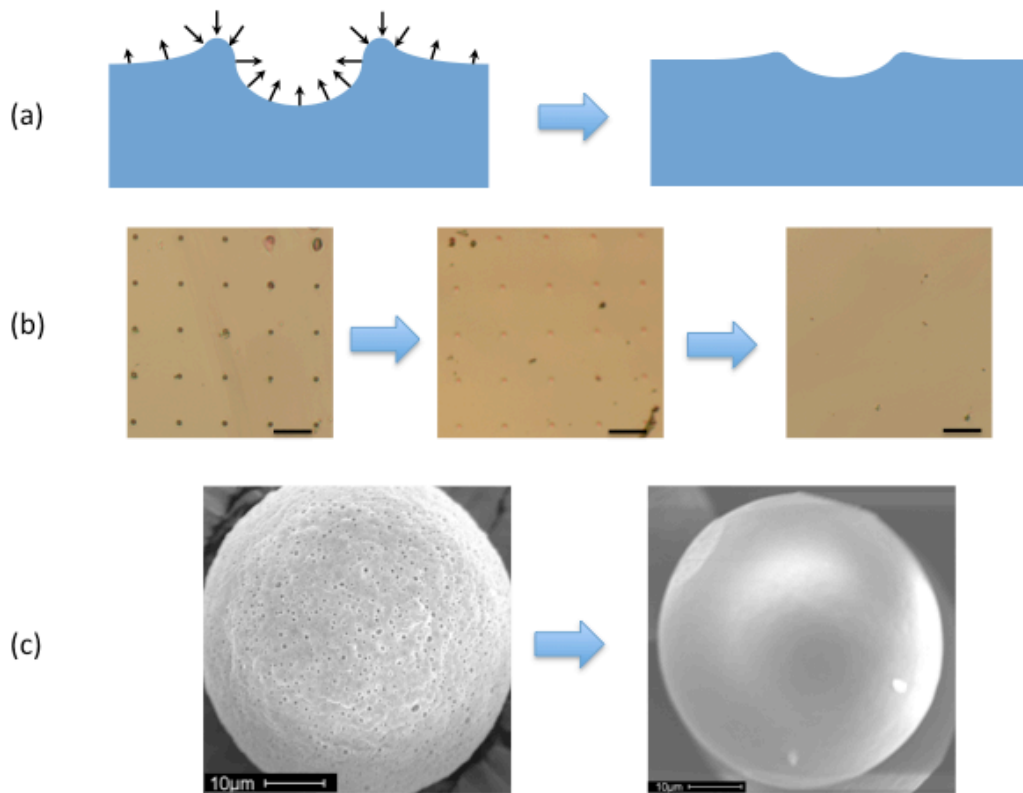


**Figure 1** Self-healing in PLGA. **a)** A schematic illustration of the healing process showing the shape-recovery of a surface pore driven by stress fields arising from surface curvature. The stress fields can be mimicked by the application of surface tractions that are proportional to local curvatures. **b)** Micrographs of self-healing of pores introduced by indentation of a PLGA film when incubated at 65 °C. **c)** Self-healing of surface pores in PLGA microparticles used in controlled release. The left image is after fabrication using the solvent evaporation method as previously described (9), and the right image is after incubation in solution at 42 °C (above  $T_g$ ) for 48 hours.

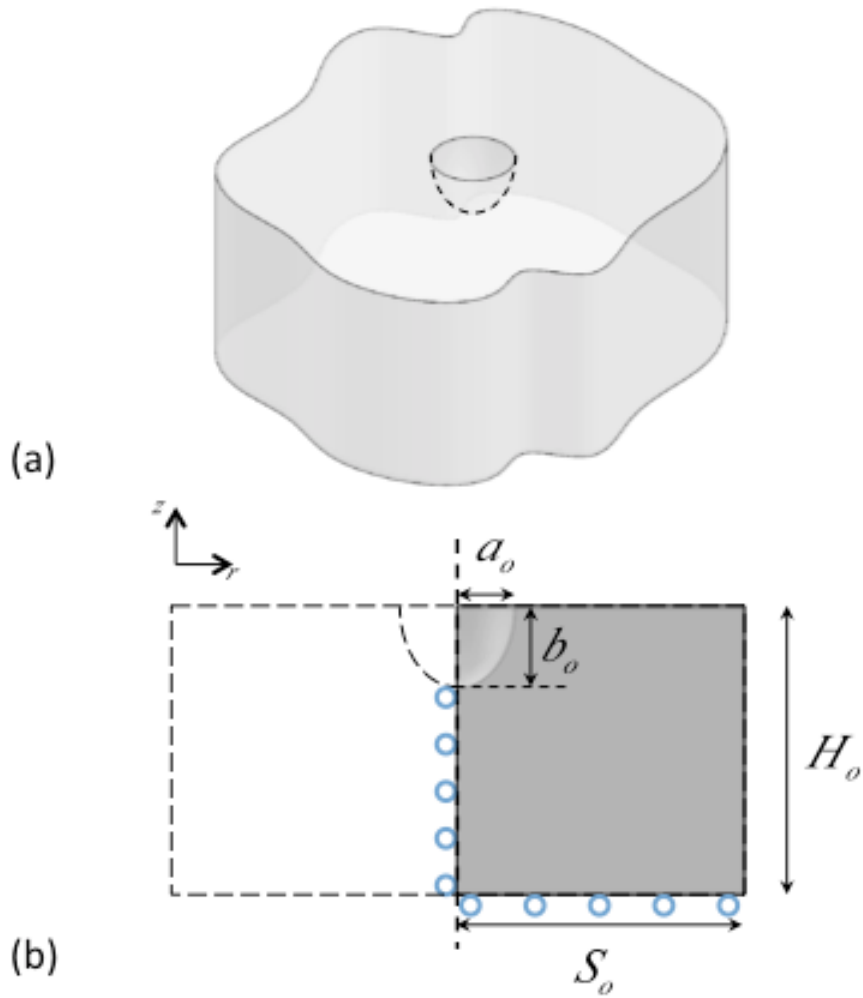


**Figure 2** a) A schematic illustration of an axisymmetric ellipsoidal surface pore. b) The axisymmetric geometry used in the numerical simulations. The boundaries are located at an outer radius of  $S_o$ , which is big enough so that the pore can be considered as an isolated pore. The thickness of the substrate is  $H_o$ . The bottom symmetry plane models free sliding on a rigid substrate.

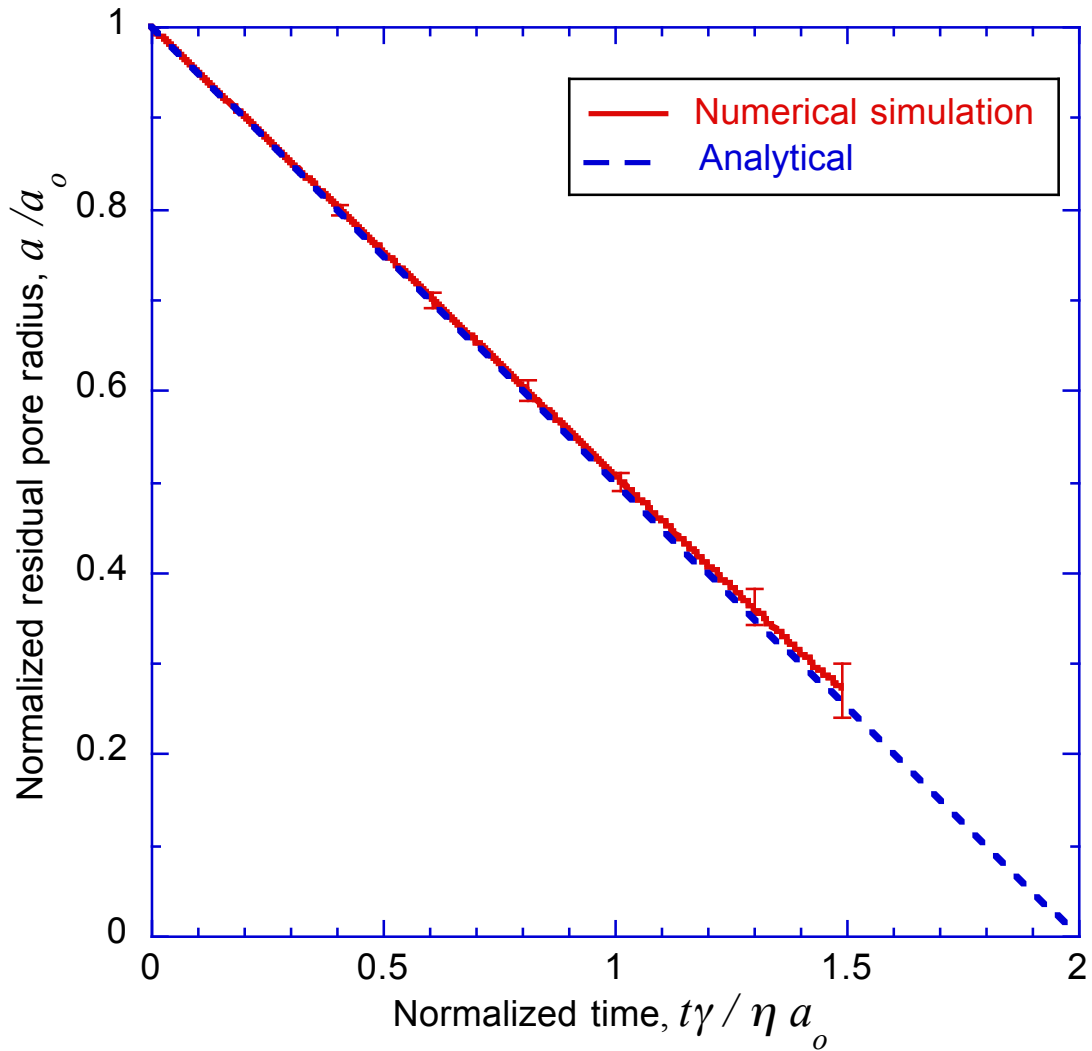


**Figure 3** The results of a numerical calculation of the healing time of a spherical pore in infinite visco-elastic body agree with the analytical results. The numerical results are affected by the excessive distortion when the residual radius of the pore is small, resulting in larger uncertainties, as represented by the error bars.

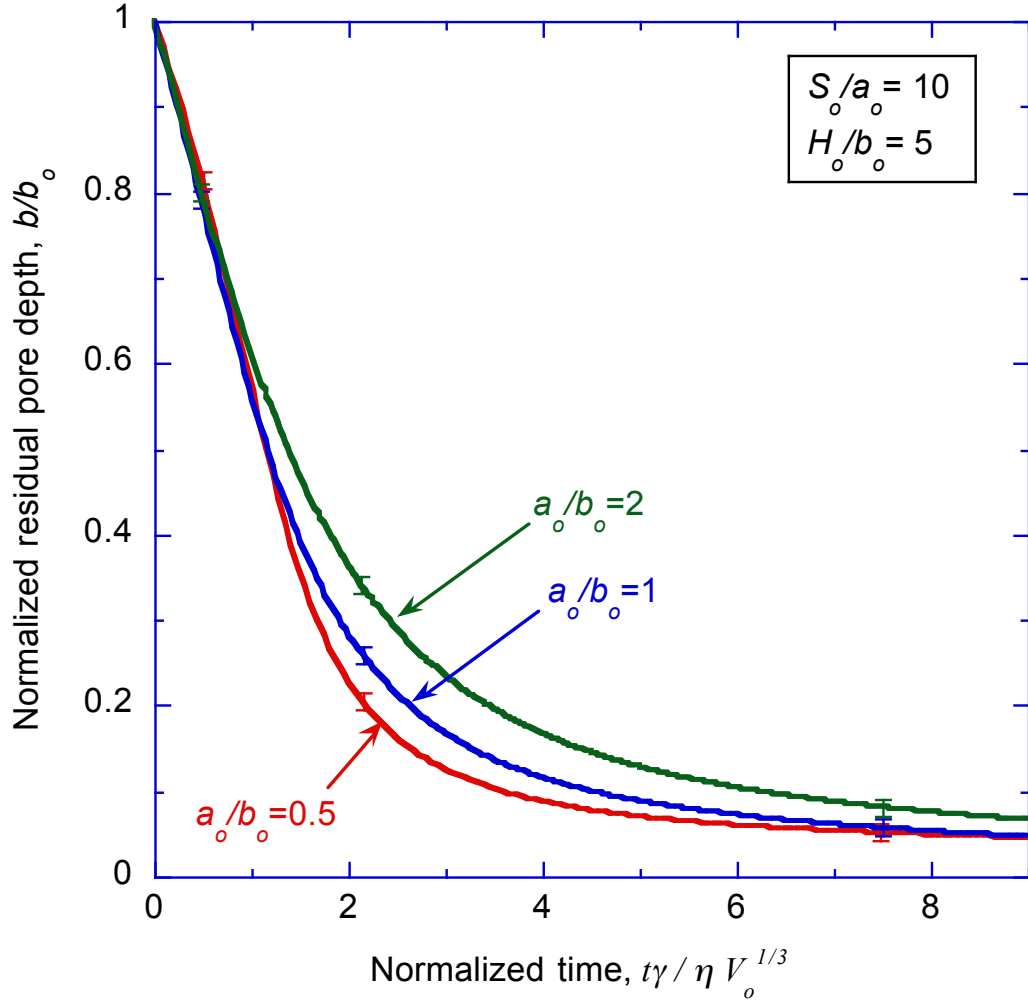


**Figure 4** (a) Numerical results showing how the residual depth of an ellipsoidal surface pore in a Maxwell material varies as a function of time; these results illustrate how the rate of healing slows down as the pore depth decreases. In this plot, the time,  $t$ , has been normalized by the surface tension,  $\gamma$  the viscosity,  $\eta$ , and the initial volume of the pore,  $V_o$ . Wider and shallower pores, of the same initial volume require longer times to reach the same level of healing. The error bars on these plots correspond to numerical uncertainties associated with mesh size. (b) Numerical results showing how the cross-sectional profile of a surface pore evolves with time. This images are taken from the simulation used to generate the data of Figure 4a, with  $a_o/b_o = 1$ .

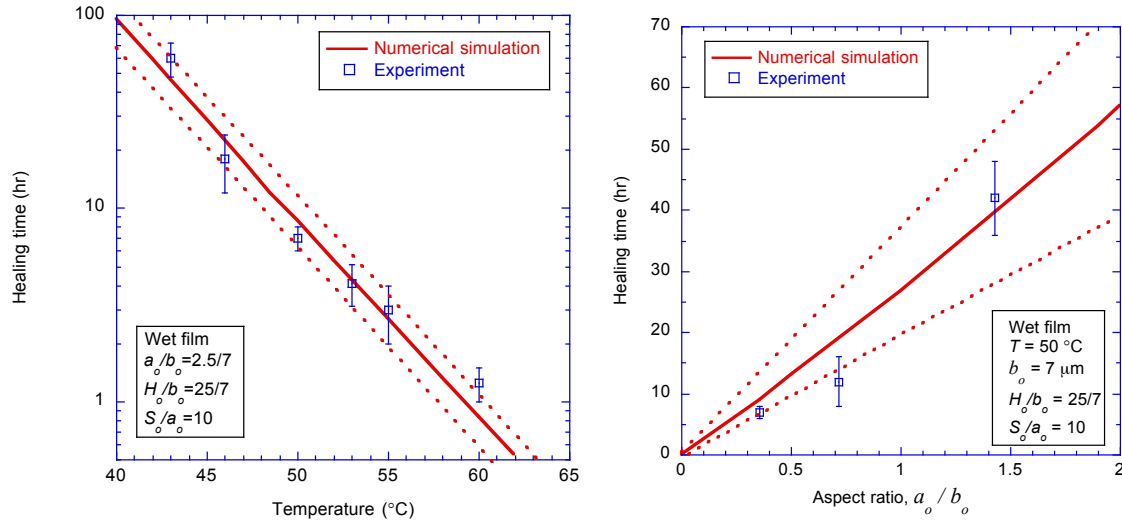


**Figure 5** (a) A comparison between the calculated time to heal pores in a wet PLGA film ( $T_g = 23.4 \pm 0.4\text{ }^\circ\text{C}$ ) and the experimental observations of Mazzara *et al.* (20), as a function of temperature. The geometrical parameters of the ellipsoidal pore used in the numerical calculations were  $a_o/b_o = 5/14$ ,  $S_o/a_o = 10$ , and  $H_o/b_o = 25/7$ . These were consistent with the experimental geometries that had pores with an initially square cross section. The material properties were chosen to fit the experimental results at  $53\text{ }^\circ\text{C}$ , and an activation energy of  $193\text{ kJ mol}^{-1}$  for the viscosity had been previously estimated from an Arrhenius fit to these data (20). The uncertainty in the numerical simulations (represented by the dashed lines) matches the uncertainty from the experimental results at  $53\text{ }^\circ\text{C}$ . (b) Good agreement is shown between the predicted and experimentally-observed effects of pore volume and aspect ratio on healing time. The experimental data are from Mazzara *et al.* [19], and the parameters for the numerical studies were identical to those used for Figure 5(a). The uncertainty in the numerical simulations (represented by the dashed lines) comes from the uncertainties to the fit in Figure 5(a).

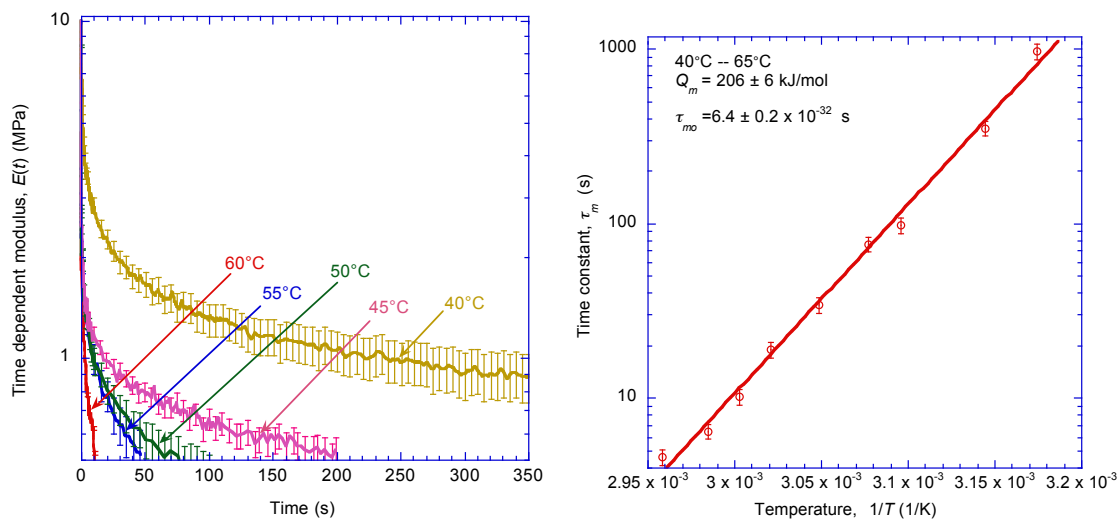


**Figure 6** (a) Sample data of stress relaxation tests for dry PLGA films at different temperatures for an initial strain of 3%, using a TA Instruments RSA3 dynamic mechanical analyzer. While the plot for a single thermally-activated relaxation is a straight line, the initial change in slope indicates additional rapid relaxation mechanisms. Only the longer-scale relaxation data were obtained from this plot. The constant slope associated with this longer time scales starts when the time-dependent modulus is  $1.5 \pm 0.5$  MPa. (b) The time constant,  $t_m$ , obtained from the data of Figure 6(a) decreases as the temperature,  $T$ , increases. An Arrhenius plot of relaxation time against  $1/T$  shows an activation energy of  $206 \pm 6 \text{ kJ mol}^{-1}$  for the viscosity term responsible for the slow relaxation in the temperature range of  $40^\circ\text{C}$  to  $65^\circ\text{C}$ . The data also indicate that the pre-exponent for the time constant (Equation 2) is given by  $t_{m0} = 6.4 \pm 0.2 \times 10^{-32} \text{ s}$ .

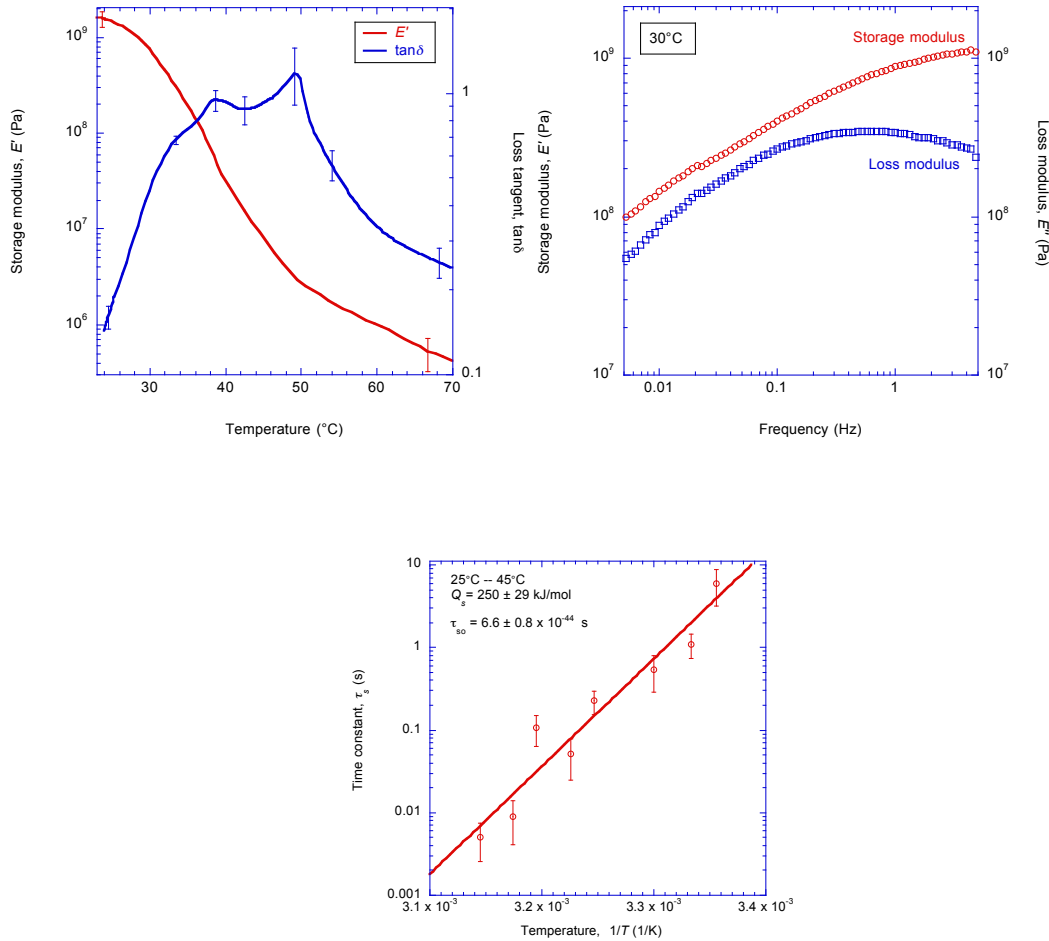


**Figure 7** (a) Temperature dependence of storage modulus and loss tangent determined by DMA for dry PLGA films. The tests were conducted at a constant frequency of 1 Hz. Three samples were tested, and the average value has been plotted. The double peaks in  $\tan \delta$  indicate at least two relaxation mechanisms with similar time constants in the temperature range, which can be approximated by one equivalent dashpot. The unrelaxed storage modulus is estimated to be  $1.6 \pm 0.3$  GPa. (b) Representative data from DMA frequency sweep test showing the storage and loss modulus as functions of frequency for dry PLGA films at 30  $^{\circ}\text{C}$ . The loss modulus presents with a single peak within the range of frequency analyzed, and can be interpreted based on a standard linear solid model. The time constant can be calculated from the peak in the loss modulus, as explained in the text. (c) The time constant obtained from data such as that shown in Fig 7b decreases as the temperature,  $T$ , increases. An Arrhenius plot shows an activation energy of  $250 \pm 29 \text{ kJ mol}^{-1}$  for the fast relaxation. The pre-exponent for the time constant (Equation 2) is given by  $\tau_{s0} = 6.6 \pm 0.8 \times 10^{-44} \text{ s}$ .

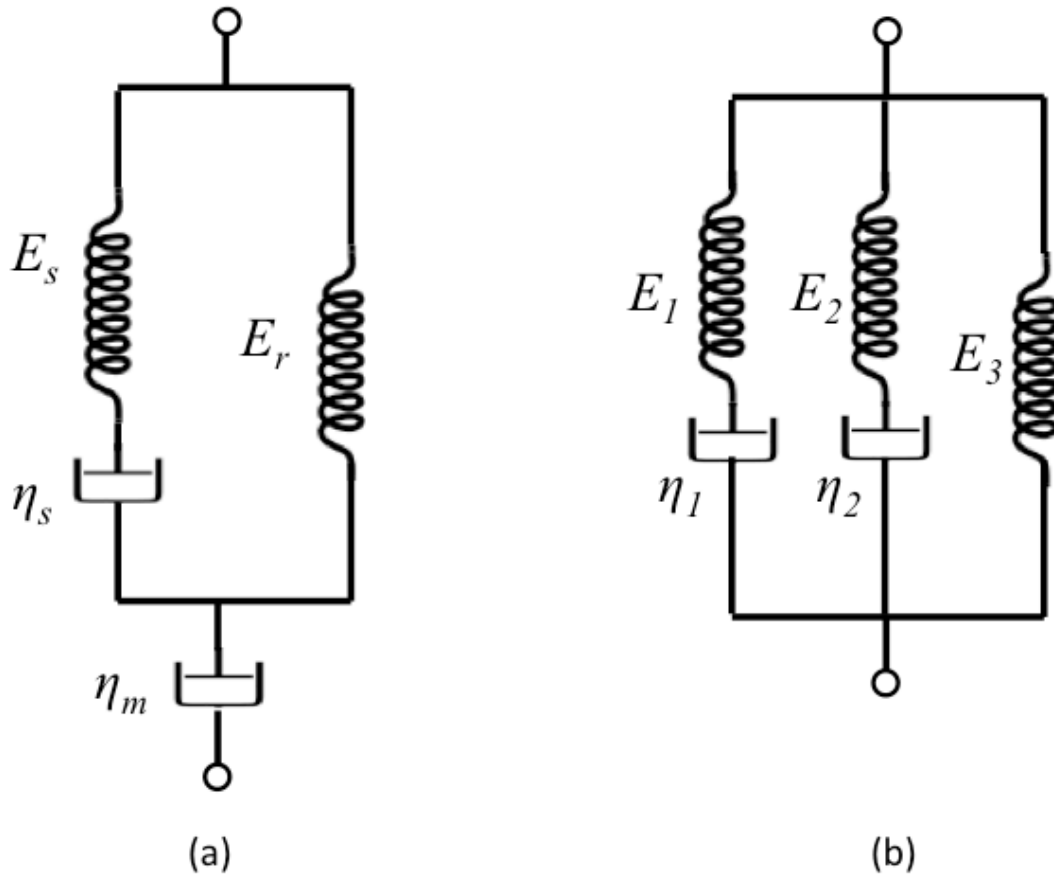


**Figure 8** Proposed material model for PLGA. **(a)** The model consists of a standard linear solid in series with a dashpot. The standard linear solid series provide a time-dependent initial modulus for the lower dashpot. The material has a fully-relaxed modulus of zero, ensuring complete healing to occur. The lower dashpot is the dominant relaxation mechanism at longer time scales. **(b)** The equivalent model used as a Prony series for finite element calculations in ABAQUS, with  $E_1 = E_s$ ,  $E_2 = E_r$ ,  $\eta_1 = (1/\eta_s + 1/\eta_m)^{-1}$ , and  $\eta_2 = \eta_m$ .  $E_3$  was arbitrarily chosen for the implementation of the Prony series, and was sufficiently small so as not to impede healing.

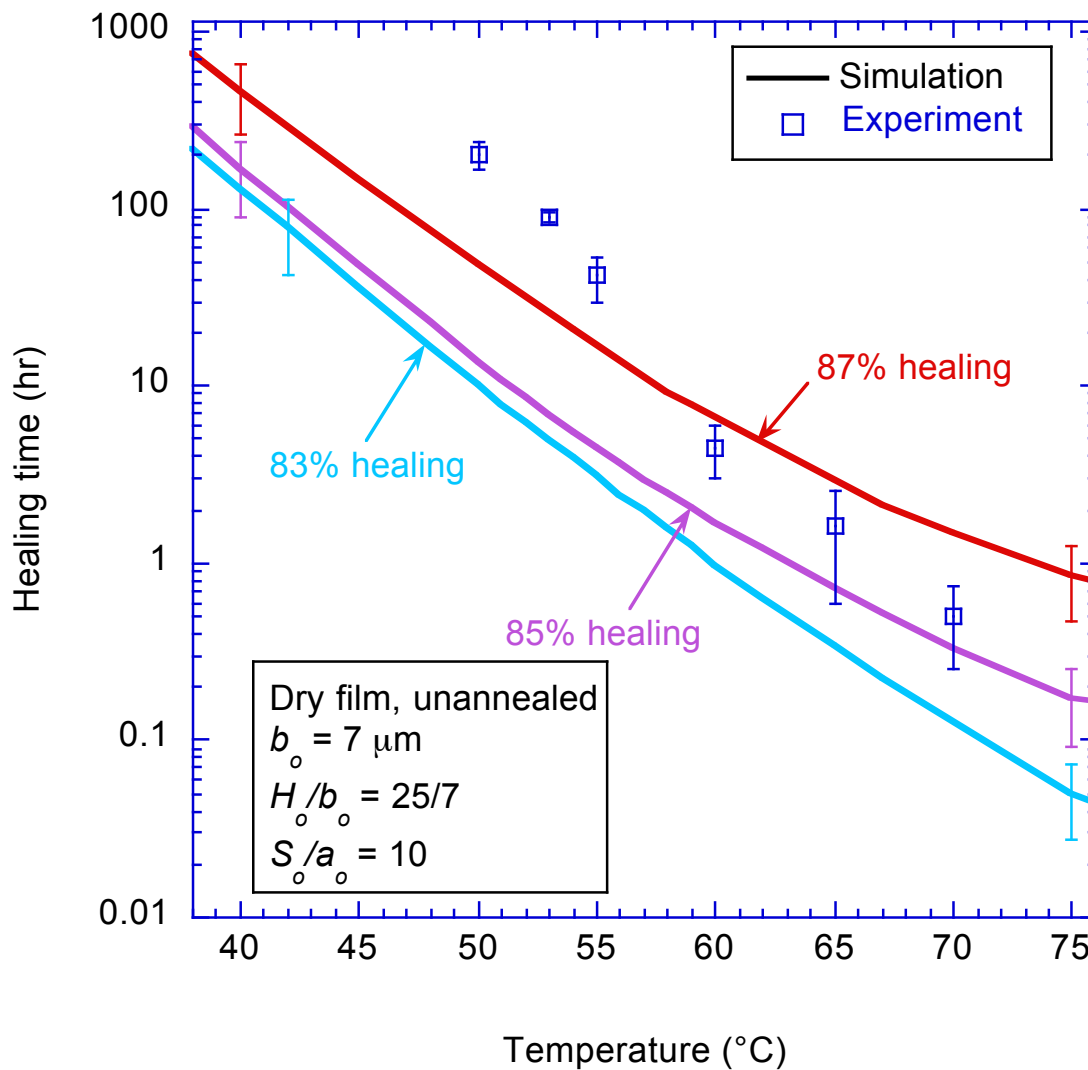


**Figure 9** The predicted time to heal a surface pore in dry PLGA films, using the material properties obtained in this study. Three different definitions of healing, 83%, 85% and 87% are shown to illustrate the sensitivity of the results to the definition of healing. The predicted results are in good agreement with the experimental observations at high temperatures, but predict too short a healing time at lower temperatures.

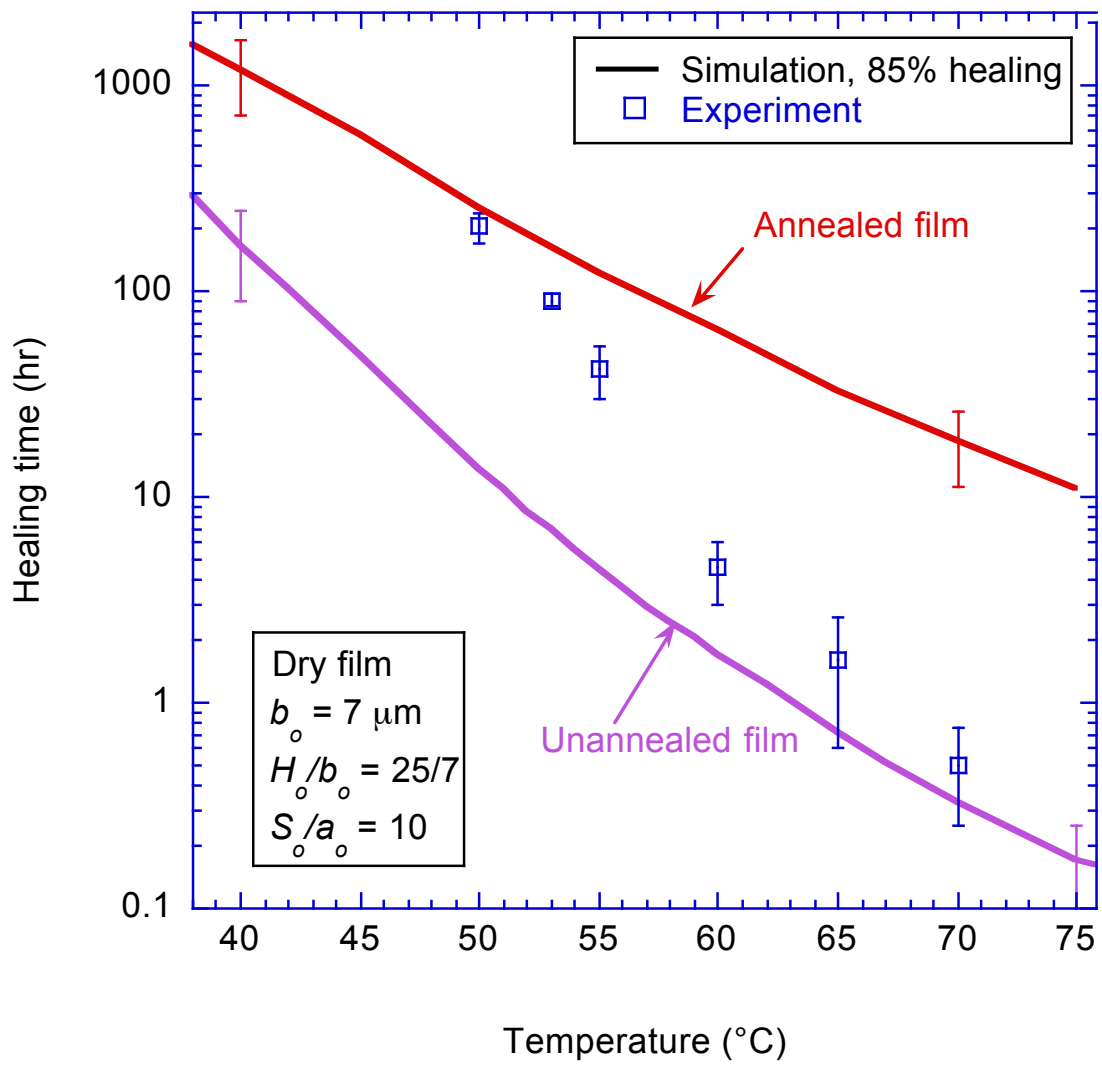


**Figure 10** The predicted time to heal a surface pore in annealed PLGA films, using the annealed properties of the PLGA. The annealed properties provide a better match for the predictions at low temperatures, while the un-annealed properties provide a better match at higher temperatures. This is consistent with the notion that the long healing times at low temperatures allow annealing to occur, and the corresponding loss of solvent reduces the viscosity of the PLGA.

### Supplementary Data

**Figure S1** The weight of dry PLGA films measured as a function of time when held at 50 °C, 55 °C and 65 °C. The relative weight change percentage of evaporated solvent after 8 hours of treatment was  $1.9 \pm 0.2\%$ .

**Supplementary Movie 1:** Simulated healing of a surface pore in a Maxwell film. The pore geometry used was  $a_o/b_o=1$ . The corresponding pore depth as a function of time can be found in Figure 4a.

([http://www-personal.umich.edu/~thouless/Huang\(2015\)-movie.mov](http://www-personal.umich.edu/~thouless/Huang(2015)-movie.mov))

Supplemental Figure 1

